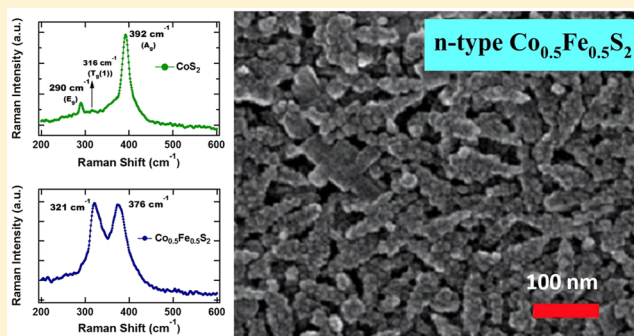


Majority Carrier Type Control of Cobalt Iron Sulfide ($\text{Co}_x\text{Fe}_{1-x}\text{S}_2$) Pyrite Nanocrystals

Tyler Kinner,^{†,‡,§,||} Khagendra P. Bhandari,^{†,||} Ebin Bastola,[†] Bradley M. Monahan,^{‡,⊥} Neale O. Haugen,^{†,#} Paul J. Roland,[†] Terry P. Bigioni,^{†,‡} and Randy J. Ellingson^{*,†}

[†]Wright Center for Photovoltaics Innovation and Commercialization, Department of Physics and Astronomy, School for Solar and Advanced Renewable Energy, and [‡]Department of Chemistry, The University of Toledo, Toledo, Ohio 43606, United States

ABSTRACT: We report the colloidal synthesis, characterization, and electronic property control of compositionally varied $\text{Co}_x\text{Fe}_{1-x}\text{S}_2$ cubic pyrite nanocrystals (NCs) and thin films formed from solution. Using drop-cast NC thin films, we demonstrate the relationship between the material composition and the majority carrier type of the nanocrystalline thin films. Measurements of the majority carrier type as a function of NC composition indicate that $\text{Co}_x\text{Fe}_{1-x}\text{S}_2$ NC thin films change from p-type to n-type between $x = 0.16$ and $x = 0.21$. Additional characterization to confirm the crystallinity, composition, size, and shape was performed using powder X-ray diffraction, Raman spectroscopy, energy dispersive X-ray spectroscopy, and scanning electron microscopy. The observed n-type behavior which accompanies the substitution of Co for Fe in these cubic pyrite nanostructures agrees with previous reports of n-type behavior occurring at even very low concentration Co doping of iron pyrite. The ability to prepare n- or p-type pyrite NCs and thin films opens the door to property-controlled cobalt iron pyrite nanocrystalline materials for optoelectronic and energy conversion applications.



INTRODUCTION

Pyrite iron sulfide (FeS_2) is a common sulfide material that has been extensively researched for use as an effective light absorbing layer in photovoltaics (PV).^{1–7} Iron pyrite is a semiconductor with an indirect band gap of ~ 0.95 eV and an absorption coefficient over the visible spectrum of $>10^5$ cm^{-1} , which makes it a promising material for PV.^{1–3} Additionally, its abundance and benign nature make it a useful material for large-scale PV deployment.⁵ However, studies of FeS_2 thin films have consistently revealed a material plagued by crystal defects^{1,3,4,6,7} commonly believed to arise primarily from sulfur vacancies. These defects have so far prevented the application of FeS_2 as a photovoltaic absorber material. Iron and iron cobalt pyrites have been prepared by many methods, including chemical vapor deposition/transport (CVD/CVT),^{8–10} and sulfurization of iron or iron–cobalt films deposited by electrodeposition,¹¹ thermal evaporation,^{12,13} sputtering,¹⁴ and pulsed laser deposition.¹⁵ In light of the tendency for nominally stoichiometric FeS_2 pyrite films to form as sulfur-poor samples with Fe/S ratios >0.5 , even direct preparation of iron pyrite has typically required a thermal sulfurization step to achieve near-stoichiometric composition and optimal pyrite phase purity.

Relatively recently, the fabrication of iron pyrite in nanocrystalline form has renewed interest in the material.^{16–21}

Several methods of iron pyrite nanocrystal (NC) synthesis have been reported, demonstrating significant variation in the shapes and sizes of the final product. Tuning of the sizes and

shapes via modifications in the reaction temperature, time, or reagents is possible, allowing for development of unique materials with distinct properties.^{16,18–21} Thus far, solution-based syntheses of semiconductor NCs have resulted in high-quality crystalline products, but even marginally efficient photovoltaic devices have yet to be realized. Other applications for iron pyrite have recently been investigated, such as its use as an electrode in dye-sensitized PV,²² as an electrocatalyst for hydrogen evolution,²³ and at the back contact in CdTe solar cells.²⁴

Because of its multiplicity as a functional energy material, engineering of pyrite FeS_2 may allow for even greater utility, with potential to alter semiconducting properties such as band gap energy,²⁵ conductivity, and majority carrier type. Doping of iron pyrite to change the majority carrier type from p-type to n-type has been reported extensively within the literature for thin-film growth via CVD/CVT.^{3,10,26–28} Here, we present an investigation into the synthesis and properties of nanocrystalline iron pyrite alloyed with cobalt to form $\text{Co}_x\text{Fe}_{1-x}\text{S}_2$ cobalt iron pyrite. Cobalt and Fe are immediate neighbors on the periodic table, with electron configurations of $[\text{Ar}]3d^74s^2$ and $[\text{Ar}]3d^64s^2$, respectively. Cobalt disulfide is isostructural with FeS_2 pyrite and, therefore, readily forms the pyrite structure

Received: November 16, 2015

Revised: February 26, 2016

(CoS₂, cattierite); and with the cobalt atom's additional *d* shell electron as compared with Fe, the selection of Co as an n-type dopant for iron pyrite appears immediately promising. Indeed, Co has been reported as a dopant to convert FeS₂ pyrite films to n-type behavior, with doping accomplished in one case by apertured electron beam evaporation of Co directly onto CVD iron pyrite followed by thermal interdiffusion.²⁷ Oertel et al. found that CVD iron pyrite films directly incorporating Co exhibited n-type behavior for $x > 3.4 \times 10^{-3}$.¹⁰ While iron pyrite is semiconducting, cobalt's additional d-shell electron yields a ferromagnetic metal²⁹ in the case of cobalt pyrite (CoS₂, cattierite). Colloidal nanocrystalline cobalt pyrite has been synthesized by hydrothermal methods³⁰ and has recently been demonstrated as an effective counter electrode within quantum dot sensitized solar cells³¹ and as an electrocatalyst for hydrogen evolution.³²

EXPERIMENTAL METHODS

Materials. Iron(II) chloride tetrahydrate (99.99%), cobalt(II) chloride hexahydrate (98%), sulfur (98%), trioctylphosphine oxide (TOPO, 99%), and oleylamine (OLA, technical grade 70%) were obtained from Sigma-Aldrich and used without further purification.

Co_xFe_{1-x}S₂ Nanocrystal Synthesis. Cobalt iron pyrite NCs were synthesized following a previously published general synthetic procedure for preparing FeS₂ iron pyrite NCs.^{16,33} For a typical synthesis, 0.5 mmol of X²⁺ (X = Fe, Co) and 3 mmol of TOPO were added to 10 mL of OLA. The solution was degassed under alternating vacuum/vigorous N₂ flow for ~5 min. The solution was then heated to 170 °C and held for 3 h. Then, 3 mmol of sulfur in 5 mL of OLA was injected, yielding a near-instantaneous color change from dark green (consistent with FeS₂ NCs) to brown for alloy compositions and to black for CoS₂ NCs. The solution was heated to 220 °C and held for 2 h immediately following the injection of sulfur. After the 2 h growth period, the solution was removed from heat and allowed to cool. Purification was performed in air using standard nonsolvent precipitation/centrifugation techniques. After purification, the NC precipitate was redissolved in chloroform to yield a stable, uniform solution without aggregates or short-term precipitation. Solutions in chloroform were used for characterization by optical absorption spectroscopy (Figure 1).

Nanocrystal Film Preparation. Co_xFe_{1-x}S₂ NC solutions were prepared in chloroform with a concentration of ~6 mg/mL. Nanocrystal films were prepared, without further treatment, on soda-lime glass substrates or zero background silicon substrates using drop-casting or spin-casting methods. The color of the film changed from shiny golden to black as the concentration of Co increased from $x = 0$ to $x = 1$. Nanocrystal thin films thus prepared were utilized as described below for characterization by X-ray diffraction (XRD), energy dispersive spectroscopy (EDS) and Raman spectroscopy. Nanocrystalline films used for carrier type determination by hot probe and Hall effect were also prepared by treatment with a solution of 1 M hydrazine in ethanol to remove the TOPO surfactant and enhance NC–NC electronic coupling.

Characterization. Co_xFe_{1-x}S₂ NC was characterized in the form of solution and film. Absorbance spectra of NC solution were measured using PerkinElmer Lambda 1050 UV/vis/NIR spectrophotometer. For the absorbance measurements, NC solutions were prepared in chloroform at a concentration of ~0.7 mg/mL. Spectra were recorded in 2 mm path length

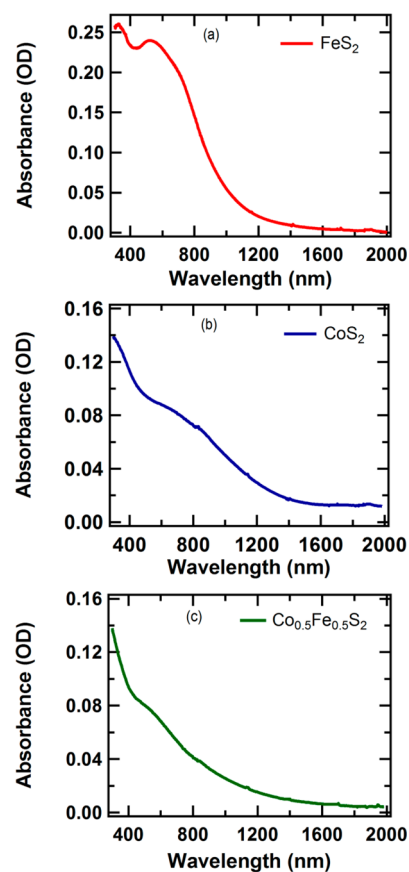


Figure 1. Absorbance spectra (optical density, OD) for the as-synthesized NCs capped with TOPO. The figures show absorbance for nanocrystalline samples consisting of (a) FeS₂, (b) CoS₂, and (c) Co_{0.5}Fe_{0.5}S₂. In all cases, the solvent was chloroform and the path length of the cuvette was 2 mm.

quartz cuvettes and were solvent corrected during the measurement.

Raman spectra were recorded for as-synthesized NC films (NC having surfactant) prepared on soda-lime glass using a laser source of wavelength 632.8 nm. Similarly, X-ray diffraction (XRD) measurements were conducted for as-synthesized NC films, deposited on zero background single-crystal Si substrates, using a Cu K α X-ray source with a wavelength of 0.15418 nm. The XRD instrument broadening of 0.08 radians fwhm was measured using a single crystal Si wafer, and subtracted from fwhm values prior to application of Scherrer analysis. Co_xFe_{1-x}S₂ NCs were prepared in various stoichiometric ratios by varying the ratio of Co/Fe in the initial reaction (X²⁺). EDS was used to confirm the composition of each Co_xFe_{1-x}S₂ sample. Hot probe measurements, which indicate the sign of the Seebeck coefficient, were conducted to identify the carrier type for NC films before and after removing the surfactant. In addition, Hall effect measurements were carried out on samples, at room temperature, using a system based on MMR Technologies' model H-50 Hall and van der Pauw controller, and model K-20 temperature controller. Samples for Hall measurements were prepared on a 1.5 cm \times 1.5 cm glass substrate, and evaporated Au contacts at the sample corners are solder-contacted by the Hall system probes. The maximum magnetic field for this system is 2kG.

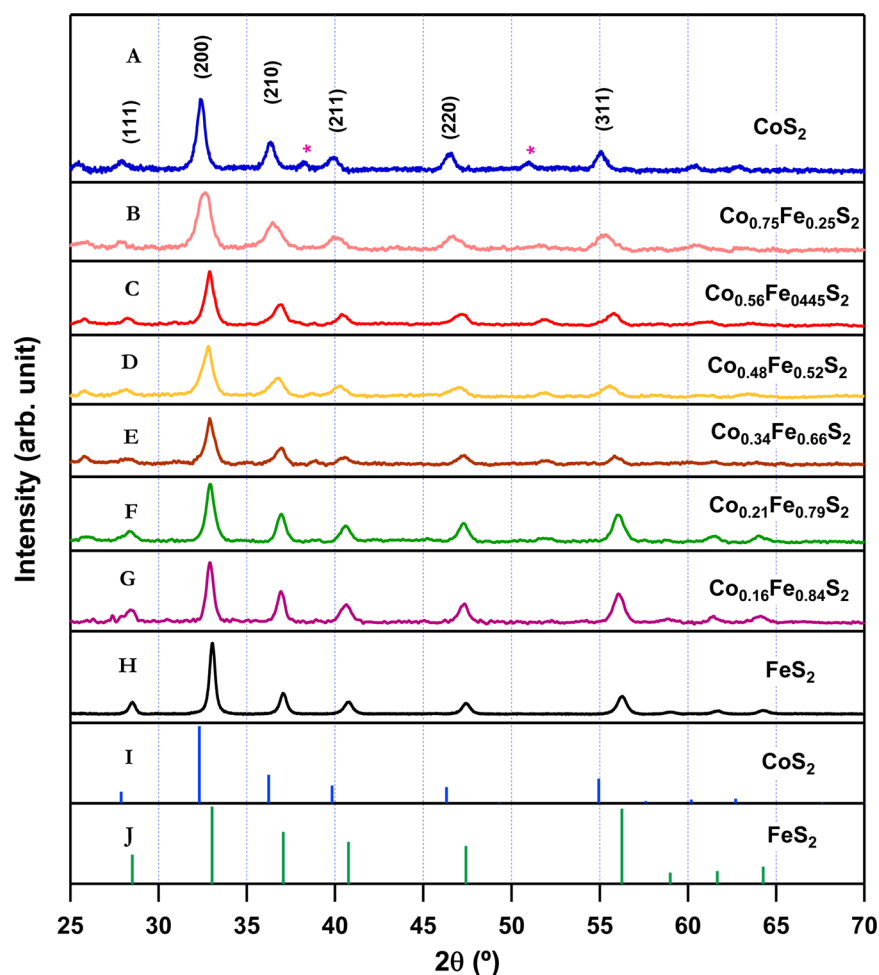


Figure 2. Powder X-ray diffraction (pXRD) patterns of FeS_2 , CoS_2 , and $\text{Co}_x\text{Fe}_{1-x}\text{S}_2$ in a variety of stoichiometric ratios, where $x = 1.0$ (A), 0.75 (B), 0.56 (C), 0.48 (D), 0.34 (E), 0.21 (F), 0.16 (G), and 0.0 (H). Vertical lines in I and J provide the reference pXRD patterns of catterite (CoS_2) and iron pyrite (FeS_2), respectively. The pink * symbols mark peaks at $2\theta = 38.2^\circ$ and $2\theta = 51.0^\circ$, tentatively assigned to Co_3S_4 phase (see text for further discussion).

RESULTS AND DISCUSSION

Figure 1 shows the optical absorbance spectra for $\text{Co}_x\text{Fe}_{1-x}\text{S}_2$ NC dispersed in chloroform. As shown in Figure 1, light absorption rises strongly for decreasing visible light wavelength for compositions $x = 0, 0.5$, and 1. The vast majority of reports on the properties of iron pyrite polycrystalline and nanocrystalline thin films show substantial optical absorption persisting well below the bandgap energy, and although Li et al.³⁴ also observe this for larger NCs, they also see relatively good crystalline iron pyrite “nanodendrimers”, which appear to exhibit much lower sub-bandgap absorption. The sub-bandgap optical absorption in semiconductors arises from disorder based on defects such as vacancies, nonimpurity lattice substitutions, nonstoichiometric composition, and impurities. For our samples, absorption of light by the FeS_2 NC sample approaches zero only at ~ 2000 nm. On the contrary, in the case of $x = 1$ (CoS_2), the sample exhibits evident absorption even at the longest wavelengths measured; the same is true for the case of $x = 0.5$, though the absorbance in this case is smaller than for the $x = 1$ case. As the composition varies from iron pyrite to catterite, optical absorption is expected to evolve based on the semiconducting nature of FeS_2 and the metallic nature of CoS_2 . Absorption of FeS_2 NC when $x = 0$ is similar to previously published results,^{16,33,34} but absorption for $x = 0.5$ and 1 cannot

be compared due to absence of such spectra in published literature.

The intended compositions were $x = 0, 0.1, 0.2, 0.3, 0.4, 0.5, 0.75$, and 1.0, while EDS indicated resulting compositions of 0.0, 0.16, 0.21, 0.34, 0.48, 0.56, 0.75, and 1.0. Based on the nanocrystalline nature of the sample, we conservatively estimate the accuracy of the composition as $\pm 5\%$; the uncertainty has been indicated within the experimental lattice constant data shown in Figure 3. The powder X-ray diffraction (pXRD) patterns obtained from diffractometer equipped with a copper X-ray source for $\text{Cu K}\alpha$ radiation ($\lambda = 1.5418 \text{ \AA}$) of each sample are shown in Figure 2. The XRD spectra measured for pure iron pyrite and for pure cobalt pyrite films are in good agreement with the corresponding XRD reference spectra. As the Co concentration increases, the XRD peak positions shift to lower 2θ values in accord with an increasing lattice constant. The accepted bulk lattice constant values for the pyrite forms of FeS_2 and CoS_2 are $5.417^{35,36}$ and 5.528 \AA ,²⁹ respectively. This gradual shift in the XRD peak positions observed is due to the increasing average lattice constant as the crystalline composition changes from pure iron pyrite to pure cobalt pyrite, as the concentration of Co is increased from 0 to unity.

Through application of Bragg’s Law, we have performed peak fitting to identify the maximum for each of the six prominent

Table 1. X-ray Diffraction Peak Positions (2θ , in degrees), and Extracted (a) and Predicted (a_0) Pyrite Lattice Constants for Eight $\text{Co}_x\text{Fe}_{1-x}\text{S}_2$ Alloy Compositions^a

x	(111)	(200)	(210)	(211)	(220)	(311)	lattice constant, a (Å)	a_0 (Å); Vegard's law
0.0 (FeS_2)	28.503	33.046	37.066	40.753	47.427	56.263	5.423 ± 0.001	5.417
0.16	28.369	32.913	36.935	40.609	47.286	56.083	5.442 ± 0.003	5.435
0.21	28.343	32.933	36.951	40.599	47.277	56.065	5.442 ± 0.005	5.440
0.34	28.225	32.919	36.894	40.526	47.260	55.906	5.452 ± 0.015	5.455
0.48	28.093	32.763	36.694	40.242	46.945	55.547	5.482 ± 0.012	5.470
0.56	28.244	32.889	36.852	40.437	47.111	55.749	5.460 ± 0.009	5.479
0.75	27.885	32.590	36.513	40.063	46.699	55.280	5.511 ± 0.016	5.500
1.0 (CoS_2)	27.925	32.403	36.345	39.878	46.490	55.066	5.530 ± 0.004	5.528

^aThe uncertainty in 2θ peak locations fell typically in the range of ± 0.002 to ± 0.005 ; the uncertainty in the derived lattice constant values corresponds to the standard deviation of the average deduced lattice constant based on 2θ values.

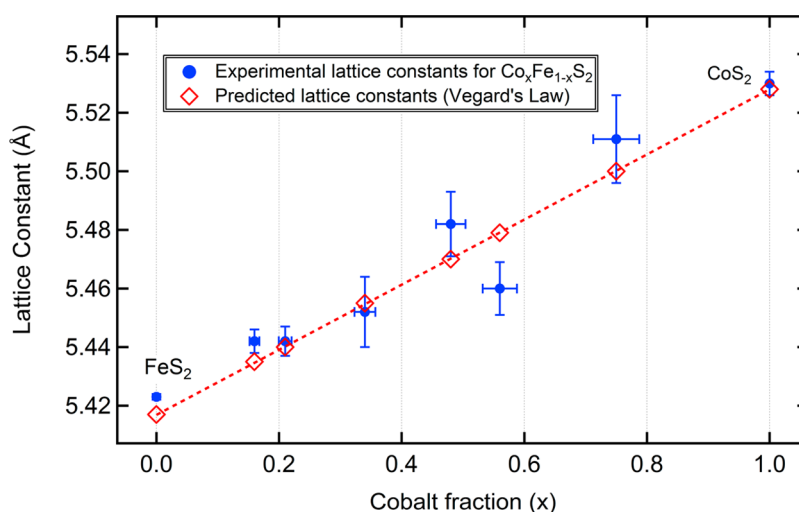


Figure 3. Lattice constants for eight compositions of $\text{Co}_x\text{Fe}_{1-x}\text{S}_2$ pyrite nanocrystals. Vertical error bars indicate the standard deviation in lattice parameter based on single spectrum fits to six peaks corresponding to Miller indices (111), (200), (210), (211), (220), and (311) in the pyrite cubic structure.

(hkl) peaks identified in Figure 2; subsequently, we have used the 2θ peak locations to calculate the lattice constant and standard deviation for each sample (see Table 1 and Figure 3). The XRD peaks near 38° and 51° observed for CoS_2 are tentatively ascribed to the presence of Co_3S_4 (linnaeite) phase which relates directly to the isometric hexoctahedral structure of Fe_3S_3 (greigite).³⁷ Related peaks are observed in the XRD spectra down to approximately $x = 0.34$. These phases, if ultimately attributed to the same crystalline structure (linnaeite/greigite), would fit the form of $\text{Co}_y\text{Fe}_{3-y}\text{S}_4$, where $0 < y < 3$. The suspected linnaeite-phase peaks follow the shift to smaller 2θ for increasing Co concentration.

As an additional check of the phase and structural purity of $\text{Co}_x\text{Fe}_{1-x}\text{S}_2$ NC samples, Raman scattering measurements were carried out using a HeNe laser (632.8 nm). Figure 4 presents Raman spectra of NC samples of FeS_2 , CoS_2 , and $\text{Co}_x\text{Fe}_{1-x}\text{S}_2$ NCs when $x = 0, 1.0$, and 0.5 ± 0.08 . The Raman spectrum from the pure FeS_2 NC film showed characteristic peaks at 341, 377, and 425 cm^{-1} respectively. The FeS_2 peaks match well with previously reported values for pyrite FeS_2 .^{16,33,38} Similarly, the Raman scattering spectrum from pure CoS_2 NC film exhibits major characteristic peaks at 290 and 392 cm^{-1} at room temperature. These values are in close agreement with literature reports for CoS_2 thin films. Zhu et al. found characteristic peaks at 287 and 389 cm^{-1} from commercial CoS_2 powder,³⁹ whereas Lyapin et al.⁴⁰ found characteristic

peaks at exactly the same locations, as obtained in this work. The Raman spectrum for the $\text{Co}_{0.5}\text{Fe}_{0.5}\text{S}_2$ NC sample differs from a simple combination of Raman spectra obtained from the CoS_2 and FeS_2 NC films, indicating that the Co^{2+} substitutes stoichiometrically for Fe^{2+} on the NC pyrite lattice.⁴¹ For $x = 0.5$, twin peaks are observed at frequencies 321 and 376 cm^{-1} . As compared with the most prominent peaks appearing in the FeS_2 and CoS_2 spectra, the two peaks for $\text{Co}_{0.5}\text{Fe}_{0.5}\text{S}_2$ are noticeably broadened, in agreement with a degree of compositional or structural disorder. Note that the presence of phases within the linnaeite/greigite group may contribute the broadening of the peaks. Based on the work of Anastassakis and Perry,⁴² the peak at 376 cm^{-1} likely represents the evolution of the 377 cm^{-1} peak observed here in FeS_2 at 377 cm^{-1} , and this peak would be expected to remain prominent and relatively stationary with compositions $x < 0.5$.

Scanning electron microscopy imaging (Figure 5) reveals smaller NCs with increasing Co content. Pure FeS_2 NCs exist here as cubes with $\sim 80 \text{ nm}$ edge length. Incorporation of Co decreased the crystallite sizes and resulted in growth patterns suggesting chain-like aggregation during synthesis or subsequent processing. Shapes of CoS_2 NCs shown in Figure 5b are similar to the work by Srouji et al. work who fabricated CoS_2 film using single source route. Estimation of crystal size from pXRD patterns was performed using the Scherrer approach (Table 2).⁴³ Even for the undoped FeS_2 sample, the calculated

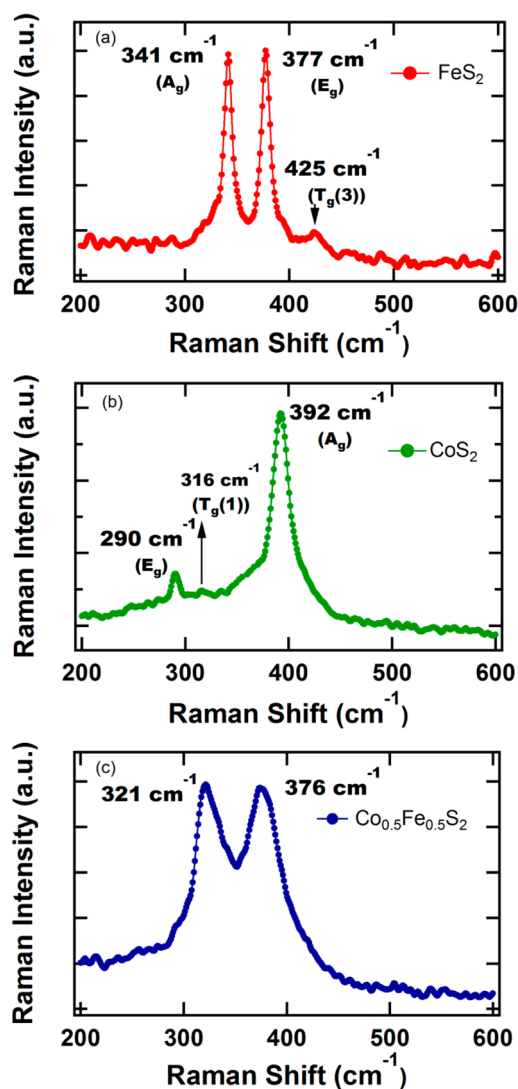


Figure 4. Raman spectra of $\text{Co}_x\text{Fe}_{1-x}\text{S}_2$ NC films measured with HeNe laser ($\lambda = 632.8$ nm); samples were prepared on soda-lime glass substrate using NC solution dispersed in chloroform.

average grain sizes appear smaller than the observed particles, indicating the likelihood that each NC consists of multiple grains. Peak fitting and analyses were performed using IgorPro

Table 2. Grain Size Based on Scherrer Analysis and Majority Carrier Type Based on Thermoprobe (HPP) Measurements of $\text{Co}_x\text{Fe}_{1-x}\text{S}_2$ Thin Films^a

material composition	avg grain size (Å) based on four Miller indices (<i>hkl</i>)				avg \pm SD	majority carrier type
	(200)	(210)	(211)	(311)		
FeS_2	244	201	181	158	196 ± 36	p
$\text{Co}_{0.16}\text{Fe}_{0.84}\text{S}_2$	190	185	152	138	176 ± 21	p
$\text{Co}_{0.21}\text{Fe}_{0.79}\text{S}_2$	152	165	143	129	153 ± 11	n
$\text{Co}_{0.48}\text{Fe}_{0.52}\text{S}_2$	139	140	144	158	141 ± 3	n
$\text{Co}_{0.56}\text{Fe}_{0.44}\text{S}_2$	108	92	88	105	96 ± 11	n
$\text{Co}_{0.66}\text{Fe}_{0.34}\text{S}_2$	139	109	105	126	118 ± 19	n
$\text{Co}_{0.75}\text{Fe}_{0.25}\text{S}_2$	96	79	94	101	90 ± 9	n
CoS_2	153	137	152	151	147 ± 9	n

^aXRD instrument broadening of 0.08 radians was subtracted from XRD peak FWHM prior to application of Scherrer analysis.

software. The results of the fit account for instrument broadening of the XRD peaks by $2\theta = 0.08$ radians.

As an initial test of the majority carrier type dependence on Co content, hot point probe measurements were performed on the series of thin-films fabricated from NCs with varying Co concentrations. The hot-probe method (HPP, also known as the thermoprobe technique) is a qualitative measurement of the thermoelectric effect, and the effect can be quantified by the Seebeck coefficient measurement method. The HPP method measures the voltage induced between two probes, one unheated and one heated, to enable rapid distinction between n-type and p-type transport within semiconductor thin films of sufficiently large carrier density. The heated probe is connected to the positive terminal of the voltmeter and the room temperature probe contacts the film ~ 2 mm away and is connected to the negative terminal of the meter. This method utilizes thermally activated diffusion of charge carriers to determine the majority carrier type.⁴⁴ The sign of the voltage created between this heated probe and a room temperature probe depends upon the majority carrier type. When two probes are applied to an n-type semiconductor, a positive voltage is induced, and vice versa for a p-type semiconductor.^{45,46} Successful hot probe measurements were carried out on the same series of $\text{Co}_x\text{Fe}_{1-x}\text{S}_2$ NCs, and the films exhibited n-type behavior for $x \geq 0.21$ and p-type behavior for $x < 0.21$. Due to the relative scarcity of literature

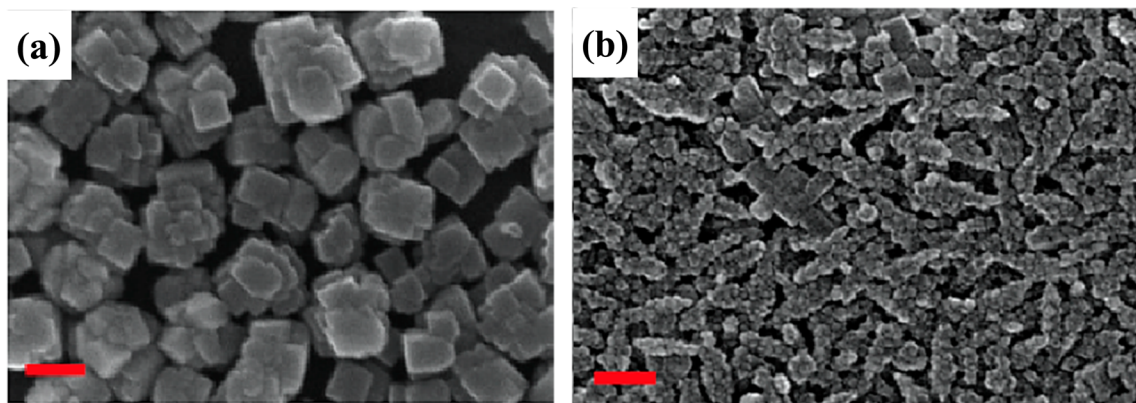


Figure 5. SEM image of pure FeS_2 NCs (a) and SEM image of $\text{Co}_{0.5}\text{Fe}_{0.5}\text{S}_2$ NCs (b). The red scale bars are 100 nm and the observed decrease in crystallite size indicated by the pXRD pattern can be seen in the SEM images.

Table 3. Hall Measurement Parameters for $\text{Co}_x\text{Fe}_{1-x}\text{S}_2$ NC Films

$\text{Co}_x\text{Fe}_{1-x}\text{S}_2$ NC	FeS_2 as-synthesized	FeS_2 hy-treated	$\text{Co}_{0.5}\text{Fe}_{0.5}\text{S}_2$ as-synthesized	$\text{Co}_{0.5}\text{Fe}_{0.5}\text{S}_2$ hy-treated	CoS_2 as-synthesized	CoS_2 hy-treated
Hall parameters						
Resistivity (Ω cm)	5.9 ± 0.5	1.7 ± 0.3	1.6 ± 0.1	0.15 ± 0.05	54.2 ± 8.7	0.10 ± 0.03
Mobility (cm^2/Vs)	0.3 ± 0.15	0.2 ± 0.12	-0.4 ± 0.04	-0.45 ± 0.27	-1.6 ± 0.28	-0.9 ± 0.17
Charge density (cm^{-3})	$4.9(\pm 1.3) \times 10^{18}$	$2.4(\pm 1.2) \times 10^{19}$	$-3.1(\pm 0.5) \times 10^{19}$	$-1.4(\pm 0.6) \times 10^{20}$	$-5.3(\pm 0.5) \times 10^{16}$	$-1.0(\pm 0.3) \times 10^{20}$
Hall coeff. ($\text{cm}^3/\text{Coul.}$)	$+2.3 \pm 0.6$	$+0.3 \pm 0.15$	-0.6 ± 0.08	-0.05 ± 0.03	-82.3 ± 8.6	-0.1 ± 0.03
Sheet resist. (Ω cm^2)	$9.4(\pm 1.4) \times 10^4$	$2.0(\pm 0.3) \times 10^4$	$4.7(\pm 0.3) \times 10^4$	$3.9(\pm 1.3) \times 10^3$	$9.3(\pm 1.4) \times 10^5$	$1.8(\pm 0.5) \times 10^4$
Carrier type	holes	holes	electrons	electrons	electrons	electrons

examples of the HPP measurement and the need for additional theoretical underpinning and evidence for reliability of the HPP method across varying materials and morphologies, we have conducted Hall effect measurements to further investigate the majority carrier type.

Hall effect characterization provides another method for determination of majority carrier type. However, in polycrystalline and nanocrystalline films, grain boundary density is high and transport may be based on hopping between NCs rather than on mobility-band transport. In such situations, Hall effect measurements often return very low and therefore unreliable values for the Hall coefficient (R_H), which arises from measurement of the induced Hall voltage. Based on the relatively large R_H values measured here and also to evidence from a device-based test described below, we believe that the Hall measurement results are valid for these samples.

Our NC films have been prepared both with and without the TOPO surfactant present during synthesis. Here and in a previous publication,³³ room temperature Hall effect measurements have been carried out for pyrite films composed of FeS_2 , $\text{Co}_{0.5}\text{Fe}_{0.5}\text{S}_2$, and CoS_2 NCs, using both untreated films and films that were hydrazine-treated to remove the TOPO surfactant molecules. Results of the Hall characterization are shown in Table 3. The films measured showed relatively high net carrier concentration, with p ranging from $\sim 10^{18}$ cm^{-3} to $\sim 10^{19}$ cm^{-3} for undoped FeS_2 , and $\text{Co}_{0.5}\text{Fe}_{0.5}\text{S}_2$ exhibiting n in the range of $\sim 10^{19}$ cm^{-3} to $\sim 10^{20}$ cm^{-3} . The CoS_2 NC films showed a larger range of values for n , from $\sim 7 \times 10^{16}$ cm^{-3} to $\sim 5 \times 10^{19}$ cm^{-3} , depending on the inclusion of hydrazine treatment. The R_H values fall mostly in the range of $\sim 10^{-1}$ to 10^0 cm^3/C . Zhang et al.⁴⁷ studied FeS_2 pyrite films prepared at varying sulfidation temperatures, and found that conventional transport occurred for those films exhibiting R_H values of approximately 10^{-2} cm^3/C , while samples prepared at lower sulfidation temperatures (≤ 450 $^\circ\text{C}$) exhibited R_H values of $\sim 5 \times 10^{-4}$. Similarly, Ares et al. noted the potential difficulty encountered with Hall measurements on samples with near-zero R_H magnitude.⁴⁸ We find that, for our samples, the R_H values are relatively large ($R_H > \sim 5 \times 10^{-2}$), supporting the validity of the Hall measurements for determination of carrier type. We note that the Hall characterization results obtained for the untreated CoS_2 film appear to be anomalous, showing very low free electron concentration; efforts are underway to repeat this measurement.

We have previously conducted both Hall measurements and temperature-dependent conductivity measurements on undoped (pure) FeS_2 NC thin films.³³ These measurements on undoped nanocrystalline FeS_2 , which also included HPP tests, have consistently indicated p-type majority carriers as shown in Table 3. The temperature-dependent resistivity measurements of our FeS_2 -NC films do not cover a sufficient range to conclusively establish the carrier transport mechanism; they show concurrence with a Werner transport model based on tunneling or thermally activate hopping across a distribution of barrier heights at inter-NC boundaries. However, we note here a conclusive check of consistency for the carrier type of our FeS_2 -NC films: we have utilized the FeS_2 -NC thin films (1 μm thick) at the back contact to CdS/CdTe solar cells.²⁴ The tested device architecture consisted of glass/TCO/CdS/CdTe/ FeS_2 -NC/Au. The result of current versus voltage characterization (dark and under AM1.5G simulated solar illumination) demonstrated that the p-CdTe/ FeS_2 -NC interface acts as a p/p+ interface, and similar behavior was observed for the as-synthesized (untreated) FeS_2 -NC films at the CdTe back contact, indicating that they too are p-type. Specifically, if the p-CdTe/ FeS_2 interface were instead functioning as a p-n junction, then for applied bias voltages positive of the open circuit voltage, the back contact diode would enter strong reverse bias and show current limiting associated with the opposing diode. Instead, a low series resistance is observed when the solar cell enters strong forward bias.²⁴

As indicated above, numerous literature reports ascribe the doping or alloying of iron pyrite with cobalt to the conversion of p-type conductivity to n-type. Deducing the majority carrier type as a function of the $\text{Co}_x\text{Fe}_{1-x}\text{S}_2$ composition for our films has been based on results of HPP and Hall measurements, and also on the low contact resistance at the back contact to p-CdTe. Ares et al. addressed the determination of the majority carrier type in iron pyrite films, explaining the improved reliability of Seebeck coefficient measurements as compared with Hall measurements.⁴⁸ The same authors have very recently addressed the influence of Co doping on the band scheme of FeS_2 . They find that whereas FeS_2 exhibits an acceptor level located 110 meV above the valence band edge, arising from iron vacancies, a broad donor level arises slightly below the conduction band edge ($E = 80 \pm 50$ meV) with the gradual replacement of Fe by Co.¹³ This recent study presents results of Seebeck coefficient results for Co-doped iron pyrite films and presents results showing that for their $\text{Co}_x\text{Fe}_{1-x}\text{S}_2$ samples

convert from p-type to n-type for $x > 0.08$. Our studies have found that the p to n transition occurs within the range of $0.16 < x < 0.21$, in reasonable agreement considering the expected variability in precise M/S ratio as well as structural variations.

CONCLUSION

We have demonstrated the successful synthesis and characterization of $\text{Co}_x\text{Fe}_{1-x}\text{S}_2$ NCs for six alloyed compositions plus iron pyrite FeS_2 and catterite CoS_2 . X-ray diffraction supports a consistent pyrite crystal structure, with alloy lattice constants that change linearly with Co fraction from FeS_2 to CoS_2 , in good agreement with Vegard's law. Crystal size calculations using the Scherrer equation show a decrease in crystallite (grain) size with increasing cobalt content. However, we have not attempted to modify reaction conditions from those used successfully in the preparation of undoped FeS_2 pyrite NCs. Adjustment of reaction conditions would likely allow for some control of NC size, shape, and tendency to aggregate. Additionally, in comparison to FeS_2 NCs, $\text{Co}_x\text{Fe}_{1-x}\text{S}_2$ NCs synthesized were significantly smaller, and CoS_2 NCs exhibited a chain-like morphology/shape not witnessed in previous literature. Hot point probe and hall measurements indicate that as the Co fraction increases, the thin films change from exhibiting p-type behavior to n-type behavior at or below 21% Co fraction. These studies serve as a guide to further investigations of electronic properties of nanocrystalline cobalt iron sulfide, and to the preparation of doped metal chalcogenide NCs, a class of materials that continues to receive significant attention for energy conversion applications.

AUTHOR INFORMATION

Corresponding Author

*E-mail: randy.ellingson@utoledo.edu.

Present Addresses

[§]Tyler Kinner, Woodrow Wilson Fellowship, Atlanta, GA.

[†]Brad Monahan, First Solar, Perrysburg, OH.

[#]Neale Haugen, Dynetech LLC, Toledo, OH.

Author Contributions

^{||}These authors contributed equally to this work.

Notes

The authors declare no competing financial interest.

ACKNOWLEDGMENTS

T.K. was supported by the National Science Foundation's Research Experience for Undergraduates program under Grant Nos. PHY-1004649 (2012) and PHY-1262810 (2013). K.P.B., E.B., B.M.M., T.P.B., and R.J.E. were supported by the National Science Foundation's Sustainable Energy Pathways Program under Grant CHE-1230246. K.P.B., P.J.R., and R.J.E. acknowledge support for this work from the United States Air Force Research Laboratory, Space Vehicles Directorate under Contracts #FA9453-08-C-0172 and #FA9453-11-C-0253.

REFERENCES

- Chatzitheodorou, G.; Fiechter, S.; Könenkamp, R.; Kunst, M.; Jaegermann, W.; Tributsch, H. Thin Photoactive FeS_2 (Pyrite) Films. *Mater. Res. Bull.* **1986**, *21*, 1481–1487.
- Ennaoui, A.; Tributsch, H. Iron Sulphide Solar Cells. *Sol. Cells* **1984**, *13*, 197–200.
- Ennaoui, A.; Tributsch, H. Energetic Characterization of the Photoactive FeS_2 (Pyrite) Interface. *Sol. Energy Mater.* **1986**, *14*, 461–474.

(4) Smestad, G.; Ennaoui, A.; Fiechter, S.; Tributsch, H.; Hofmann, W. K.; Birkholz, M.; Kautek, W. Photoactive Thin Film Semiconducting Iron Pyrite Prepared by Sulfurization of Iron Oxides. *Sol. Energy Mater.* **1990**, *20*, 149–165.

(5) Wadia, C.; Alivisatos, A. P.; Kammen, D. M. Materials Availability Expands the Opportunity for Large-Scale Photovoltaics Deployment. *Environ. Sci. Technol.* **2009**, *43*, 2072–2077.

(6) Nakamura, S.; Yamamoto, A. Electrodeposition of Pyrite(FeS_2) Thin Films for Photovoltaic Cells. *Sol. Energy Mater. Sol. Cells* **2001**, *65*, 79–85.

(7) Takahashi, N.; Nakatani, Y.; Yatomi, T.; Nakamura, T. Growth of Single-Crystal Pyrite Films by Atmospheric Pressure Chemical Vapor Deposition. *Chem. Mater.* **2003**, *15*, 1763–1765.

(8) Berry, N.; Cheng, M.; Perkins, C. L.; Limpinsel, M.; Hemminger, J. C.; Law, M. Atmospheric-Pressure Chemical Vapor Deposition of Iron Pyrite Thin Films. *Adv. Energy Mater.* **2012**, *2*, 1124–1135.

(9) Samad, L.; Cabán-Acevedo, M.; Shearer, M. J.; Park, K.; Hamers, R. J.; Jin, S. Direct Chemical Vapor Deposition Synthesis of Phase-Pure Iron Pyrite (FeS_2) Thin Films. *Chem. Mater.* **2015**, *27*, 3108–3114.

(10) Oertel, J.; Ellmer, K.; Bohne, W.; Rohrich, J.; Tributsch, H. Growth of N-Type Polycrystalline Pyrite (FeS_2) Films by Metal-organic Chemical Vapour Deposition and Their Electrical Characterization. *J. Cryst. Growth* **1999**, *198*, 1205–1210.

(11) Pimenta, G.; Schröder, V.; Kautek, W. Thin Pyrite Films Prepared by Sulphurization of Electrodeposited Iron Films. *Berichte der Bunsengesellschaft für physikalische Chemie* **1991**, *95*, 1470–1475.

(12) Dahman, H.; Khalifa, M.; Brunel, M.; Rezig, B. Iron Pyrite Films Prepared by Sulfur Vapor Transport. *Thin Solid Films* **1996**, *280*, 56–60.

(13) Clamagirand, J. M.; Ares, J. R.; Flores, E.; Diaz-Chao, P.; Leardini, F.; Ferrer, I. J.; Sánchez, C. Influence of Temperature on Thermoelectric Properties of $\text{Fe}_x\text{Co}_{1-x}\text{S}_2$ Thin Films: A Semiconductor to Semimetal Conversion. *Thin Solid Films* **2016**, *600*, 19–24.

(14) Wan, D.; Wang, B.; Wang, Y.; Sun, H.; Zhang, R.; Wei, L. Effects of the Sulfur Pressure on Pyrite FeS_2 Films Prepared by Sulfurizing Thermally Iron Films. *J. Cryst. Growth* **2003**, *257*, 286–292.

(15) Moutis, N.; Speliotis, T.; Panagiotopoulos, I.; Ziese, M. Magnetotransport Properties of Cobalt-Iron Pyrite Films. *Thin Solid Films* **2008**, *516*, 2078–2081.

(16) Bi, Y.; Yuan, Y.; Exstrom, C. L.; Darveau, S. A.; Huang, J. Air Stable, Photosensitive, Phase Pure Iron Pyrite Nanocrystal Thin Films for Photovoltaic Application. *Nano Lett.* **2011**, *11*, 4953–7.

(17) Steinhagen, C.; Harvey, T. B.; Stolle, C. J.; Harris, J.; Korgel, B. A. Pyrite Nanocrystal Solar Cells: Promising, or Fool's Gold? *J. Phys. Chem. Lett.* **2012**, *3*, 2352–2356.

(18) Cabán-Acevedo, M.; Faber, M. S.; Tan, Y.; Hamers, R. J.; Jin, S. Synthesis and Properties of Semiconducting Iron Pyrite (FeS_2) Nanowires. *Nano Lett.* **2012**, *12*, 1977–1982.

(19) Macpherson, H. A.; Stoldt, C. R. Iron Pyrite Nanocubes: Size and Shape Considerations for Photovoltaic Application. *ACS Nano* **2012**, *6*, 8940–9.

(20) Lucas, J. M.; Tuan, C.-C.; Lounis, S. D.; Britt, D. K.; Qiao, R.; Yang, W.; Lanzara, A.; Alivisatos, A. P. Ligand-Controlled Colloidal Synthesis and Electronic Structure Characterization of Cubic Iron Pyrite (FeS_2) Nanocrystals. *Chem. Mater.* **2013**, *25*, 1615–1620.

(21) Gong, M.; Kirkeminde, A.; Ren, S. Symmetry-Defying Iron Pyrite (FeS_2) Nanocrystals through Oriented Attachment. *Sci. Rep.* **2013**, *3*, 2092.

(22) Shukla, S.; et al. Iron Pyrite Thin Film Counter Electrodes for Dye-Sensitized Solar Cells: High Efficiency for Iodine and Cobalt Redox Electrolyte Cells. *ACS Nano* **2014**, *8*, 10597–10605.

(23) Faber, M. S.; Lukowski, M. A.; Ding, Q.; Kaiser, N. S.; Jin, S. Earth-Abundant Metal Pyrites (FeS_2 , CoS_2 , NiS_2 , and Their Alloys) for Highly Efficient Hydrogen Evolution and Polysulfide Reduction Electrocatalysis. *J. Phys. Chem. C* **2014**, *118*, 21347–21356.

(24) Bhandari, K. P.; Koirala, P.; Paudel, N. R.; Khanal, R. R.; Phillips, A. B.; Yan, Y.; Collins, R. W.; Heben, M. J.; Ellingson, R. J. Iron Pyrite Nanocrystal Film Serves as a Copper-Free Back Contact

for Polycrystalline CdTe Thin Film Solar Cells. *Sol. Energy Mater. Sol. Cells* **2015**, *140*, 108–114.

(25) Hu, J.; Zhang, Y.; Law, M.; Wu, R. Increasing the Band Gap of Iron Pyrite by Alloying with Oxygen. *J. Am. Chem. Soc.* **2012**, *134*, 13216–13219.

(26) Tomm, Y.; Schieck, R.; Ellmer, K.; Fiechter, S. Growth Mechanism and Electronic Properties of Doped Pyrite (FeS₂) Crystals. *J. Cryst. Growth* **1995**, *146*, 271–276.

(27) Thomas, B.; Ellmer, K.; Bohne, W.; Röhrich, J.; Kunst, M.; Tributsch, H. Photoeffects in Cobalt Doped Pyrite (FeS₂) Films. *Solid State Commun.* **1999**, *111*, 235–240.

(28) Lehner, S. W.; Savage, K. S.; Ayers, J. C. Vapor Growth and Characterization of Pyrite (FeS₂) Doped with Co, Ni, and As: Variations in Semiconducting Properties. *J. Cryst. Growth* **2006**, *286*, 306–317.

(29) Kwon, S. K.; Youn, S. J.; Min, B. I. Itinerant Ferromagnetism in Half-Metallic CoS₂. *Phys. Rev. B: Condens. Matter Mater. Phys.* **2000**, *62*, 357–360.

(30) Chen, X.; Fan, R. Low-Temperature Hydrothermal Synthesis of Transition Metal Dichalcogenides. *Chem. Mater.* **2001**, *13*, 802–805.

(31) Faber, M. S.; Park, K.; Cabán-Acevedo, M.; Santra, P. K.; Jin, S. Earth-Abundant Cobalt Pyrite (CoS₂) Thin Film on Glass as a Robust, High-Performance Counter Electrode for Quantum Dot-Sensitized Solar Cells. *J. Phys. Chem. Lett.* **2013**, *4*, 1843–1849.

(32) Zhang, H.; Li, Y.; Zhang, G.; Xu, T.; Wan, P.; Sun, X. A Metallic CoS₂ Nanopyramid Array Grown on 3d Carbon Fiber Paper as an Excellent Electrocatalyst for Hydrogen Evolution. *J. Mater. Chem. A* **2015**, *3*, 6306–6310.

(33) Bhandari, K. P.; Roland, P. J.; Kinner, T.; Cao, Y.; Choi, H.; Jeong, S.; Ellingson, R. J. Analysis and Characterization of Iron Pyrite Nanocrystals and Nanocrystalline Thin Films Derived from Bromide Anion Synthesis. *J. Mater. Chem. A* **2015**, *3*, 6853–6861.

(34) Li, W.; Dobliger, M.; Vaneski, A.; Rogach, A. L.; Jackel, F.; Feldmann, J. Pyrite Nanocrystals: Shape-Controlled Synthesis and Tunable Optical Properties Via Reversible Self-Assembly. *J. Mater. Chem.* **2011**, *21*, 17946–17952.

(35) Finklea, S. L., III; Cathey, L.; Amma, E. L. Investigation of the Bonding Mechanism in Pyrite Using the Mossbauer Effect and X-Ray Crystallography. *Acta Crystallogr., Sect. A: Cryst. Phys., Diffr., Theor. Gen. Crystallogr.* **1976**, *32*, 529–537.

(36) Birkholz, M.; Fiechter, S.; Hartmann, A.; Tributsch, H. Sulfur Deficiency in Iron Pyrite (FeS_{2-x}) and Its Consequences for Band-Structure Models. *Phys. Rev. B: Condens. Matter Mater. Phys.* **1991**, *43*, 11926–11936.

(37) Qian, X. F.; Zhang, X. M.; Wang, C.; Xie, Y.; Qian, Y. T. The Preparation and Phase Transformation of Nanocrystalline Cobalt Sulfides Via a Toluene Thermal Process. *Inorg. Chem.* **1999**, *38*, 2621–2623.

(38) Turcotte, S. B.; Benner, R. E.; Riley, A. M.; Li, J.; Wadsworth, M. E.; Bodily, D. Application of Raman Spectroscopy to Metal-Sulfide Surface Analysis. *Appl. Opt.* **1993**, *32*, 935–938.

(39) Zhu, L.; Susac, D.; Teo, M.; Wong, K.; Wong, P.; Parsons, R.; Bizzotto, D.; Mitchell, K.; Campbell, S. Investigation of CoS₂-Based Thin Films as Model Catalysts for the Oxygen Reduction Reaction. *J. Catal.* **2008**, *258*, 235–242.

(40) Lyapin, S.; Utyuzh, A.; Petrova, A.; Novikov, A.; Lograsso, T.; Stishov, S. Raman Studies of Nearly Half-Metallic Ferromagnetic CoS₂. *J. Phys.: Condens. Matter* **2014**, *26*, 396001.

(41) Abraitis, P. K.; Patrick, R. A. D.; Vaughan, D. J. Variations in the Compositional, Textural and Electrical Properties of Natural Pyrite: A Review. *Int. J. Miner. Process.* **2004**, *74*, 41–59.

(42) Anastassakis, E.; Perry, C. H. Light Scattering and Ir Measurements in XS₂ Pyrite-Type Compounds. *J. Chem. Phys.* **1976**, *64*, 3604–3609.

(43) Scherrer, P. Bestimmung Der Größe Und Der Inneren Struktur Von Kolloidteilchen Mittels Röntgenstrahlen. *Nachr. Ges. Wiss. Göttingen* **1918**, *26*, 2.

(44) Axelevitch, A.; Golan, G. Hot-Probe Method for Evaluation of Majority Charged Carriers Concentration in Semiconductor Thin

Films. *Facta universitatis-series: Electronics and Energetics* **2013**, *26*, 187–195.

(45) Golan, G.; Axelevitch, A.; Gorenstein, B.; Manevych, V. Hot-Probe Method for Evaluation of Impurities Concentration in Semiconductors. *Microelectron. J.* **2006**, *37*, 910–915.

(46) Schroder, D. K. *Semiconductor Material and Device Characterization*; John Wiley and Sons, 2006.

(47) Zhang, X.; Manno, M.; Baruth, A.; Johnson, M.; Aydil, E. S.; Leighton, C. Crossover from Nanoscopic Intergranular Hopping to Conventional Charge Transport in Pyrite Thin Films. *ACS Nano* **2013**, *7*, 2781–2789.

(48) Ares, J. R.; Ferrer, I. J.; Sánchez, C. R. Majority Carriers in Pyrite Thin Films: An Analysis Based on Seebeck and Hall Coefficient Measurements. *Thin Solid Films* **2003**, *431–432*, 511–513.